Transonic Separated Solutions for an Augmentor Wing

Jolen Flores* and William R. Van Dalsem*
NASA Ames Research Center, Moffett Field, California

The viscous transonic flow about a multielement airfoil (augmentor wing) is simulated by coupling full-potential and direct/inverse differential boundary-layer algorithms. Solutions have been obtained for a variety of conditions and are in fair agreement with available experimental data. Typical results from this transonic augmentor-wing code (TAUG-V) require approximately 3 min of Cray-XMP CPU time. Since this viscous transonic code accounts for most of the important flow physics and is still economical, it is a practical tool for the design aerodynamicist.

Introduction

THE 18% thick augmentor wing, developed by de Havilland Aircraft of Canada,[1] is a novel concept in STOL aircraft. It is a unique geometrical arrangement of an asymmetric main airfoil and two smaller aft airfoils (Fig. 1). A slot opening for jet blowing exists at the trailing edge of the main airfoil. The shrouds form a channel-like region and, when combined with the blowing, act as a thrust augmentor. However, only the no-blowing case will be considered here. The high-lift, low-speed landing configuration of this unconventional wing has been successful in STOL applications.[2] Furthermore, in cruise configuration, it has been found to have several advantages over a more conventional single-foil section of the same overall thickness-to-cord ratio. Some of these advantages are higher drag-rise Mach number, lower form drag on the main airfoil section, and increased buffet boundaries.[3] The augmentor-wing configuration has also been viewed as a new type of powered-lift concept with significant benefits resulting from the integration of the powerplant and wing designs.[2] With proper integration of the powerplant and airframe, the penalties for transport fuel efficiencies may be overcome and, in some cases, even reversed.[4] These advantages have generated interest in the development of optimal landing and transonic cruise augmentor-wing configurations.

In a previous study,[5] transonic flow solutions over the augmentor wing were obtained using a new full-potential code called TAUG (transonic augmentor wing). TAUG utilizes a fully implicit approximate factorization scheme (AF2) to solve the transformed full-potential equation in a general, nonorthogonal, body-conforming coordinate system. Typical solutions on the Cray-1S required about 10 s of CPU time in contrast to 2 h using a Navier-Stokes algorithm.[6] The motivation for the development of TAUG was to enable the design aerodynamicist to quickly focus on a near-optimal augmentor-wing design while incurring only a small fraction of the cost of other transonic design methods.

Although the inviscid TAUG code yields fair agreement with experimental data, it cannot capture the important effects of viscosity. The objective of the present work is to upgrade the TAUG code to include an accurate model of the viscous regions. Because of the unique characteristics of the augmentor wing and the strong viscous/inviscid interaction present in this geometry, flexible and efficient viscous and viscous/inviscid interaction algorithms are required. The boundary-layer and viscous/inviscid interaction algorithms developed by Van Dalsem and Steger[7-9] have been adapted to this task.

Presented as Paper 85-5004 at the AIAA 3rd Applied Aerodynamics Conference, Colorado Springs, CO, Oct. 14-16, 1985; received Jan. 10, 1986; revision received Aug. 21, 1986.

*Research Scientist. Member AIAA.

Inviscid Algorithm and Grid Generation

The transonic airfoil analysis (TAIR) full-potential code[10] was modified to solve the multielement airfoil configuration of the augmentor-wing type. This code uses a fully implicit approximate-factorization (AF2) scheme to solve the transformed full-potential equation in a general, nonorthogonal, body-conforming coordinate system. The full-potential equation, written in strong conservation law form, is given by

$$(\rho\phi_x)_x + (\rho\phi_y)_y = 0 \tag{1a}$$

$$\rho = \left[1 - \frac{\gamma-1}{\gamma+1}(\phi_x^2 + \phi_y^2)\right]^{1/(\gamma-1)} \tag{1b}$$

where the velocity components (ϕ_x and ϕ_y) and the density ρ are nondimensionalized by the critical sound speed a and the stagnation density ρ_s, respectively; x and y are the Cartesian coordinates; and γ is the ratio of specific heats. Mass conservation is expressed by Eq. (1a) for flows that are isentropic and irrotational. To transform Eq. (1a) from the physical domain (Cartesian coordinates) into a computational domain, a general nonorthogonal, independent-variable transformation is used. This general transformation.

$$\xi = \xi(x,y) \qquad \eta = \eta(x,y) \tag{2}$$

maintains the strong conservation law form of Eq. (1a). The full-potential equation, written in the computational domain (ξ,η coordinate system), is given by

$$(\rho U/J)_\xi + (\rho V/J)_\eta = 0 \tag{3a}$$

$$\rho = \left[1 - \frac{\gamma-1}{\gamma+1}(A_1\phi_\xi^2 + 2A_2\phi_\xi\phi_\eta + A_3\phi_\eta^2)\right]^{1/(\gamma-1)} \tag{3b}$$

where

$$U = A_1\phi_\xi + A_2\phi_\eta$$

$$V = A_2\phi_\xi + A_3\phi_\eta \tag{4}$$

and

$$A_1 = \xi_x^2 + \xi_y^2$$

$$A_2 = \xi_x \eta_x + \xi_y \eta_y$$

$$A_3 = \eta_x^2 + \eta_y^2 \tag{5}$$

$$J = \xi_x \eta_y - \xi_y \eta_x \tag{6}$$

The U and V terms are the contravariant velocity components along the ξ and η directions, respectively; A_1, A_2, and A_3 metric quantities; and J the Jacobian of the transformation.

Three major modifications were required to transform the base TAIR code into the TAUG multielement airfoil code. The first involved changing the O-grid topology used in TAIR to a C-type topology with additional logic to enforce the proper flow-tangency boundary conditions at the upper and lower shroud surfaces. The second major modification was implemented to enhance the stability of the AF2 iteration scheme for a C-type topology. The last modification consisted of changing the outer boundary condition. For a complete discussion of the inviscid TAUG code, see Ref. 5.

Simulations are performed using inviscid grids generated by an adaptation of the GRAPE (grids about airfoils using Poisson's equations) program.[11,12] An example grid is displayed in Fig. 1 which consists of 106×35 points in the wraparound ξ and normal-like η directions, respectively. The grid topology about the main airfoil is of the C-type and that about each of the shrouds is of the H-type. Control of the normal spacing and orthogonality at all boundaries is accomplished by the iterative solution of two coupled Poisson differential equations. At the leading edge of each shroud, there is an H-type singularity (see Fig. 2). These singularities result in high skewness and stretching, but cause little difficulty since the geometric error introduced into the solution is minimized by differencing the flow and metric quantities consistently.[13]

Viscous and Viscous-Inviscid Algorithms

The viscous flow is modeled by solving the partial differential boundary-layer equations written in a general $\xi(x)$, $\eta(x,y)$ coordinate system:

x-momentum equation,

$$\rho[u(u_\xi \xi_x + u_\eta \eta_x) + v u_\eta \eta_y] = -\beta p_\xi \xi_x + (\mu u_\eta \eta_y)_\eta \eta_y \tag{7a}$$

Energy equation,

$$\rho c_p[u(T_\xi \xi_x + T_\eta \eta_x) + v T_\eta \eta_y]$$
$$= \beta u p_\xi \xi_x + (\kappa T_\eta \eta_y)_\eta \eta_y + \mu(u_\eta \eta_y)^2 \tag{7b}$$

Perfect-gas equation,

$$p = \rho T \tag{7c}$$

Continuity equation,

$$(\rho u)_\xi \xi_x + (\rho u)_\eta \eta_x + (\rho v)_\eta \eta_y = 0 \tag{7d}$$

where the equations are nondimensionalized as outlined in Refs. 7-9. By using a general x,y to $\xi(x)$, $\eta(x,y)$ coordinate transformation, a complex similarity transformation is avoided and a solution-adaptive grid is easily employed.

An implicit predictor-corrector algorithm is used to solve the boundary-layer equations. Streamwise marching begins by predicting estimates of u, T, ρ, v, ν, and κ. The predictor step uses first-order ξ difference operators in the x-momentum and energy equations, but for one step produces second-order accurate values. Because the predictor step only needs to be first-order accurate, any nonlinear coefficients can be lagged in ξ. A second-order accurate corrector step is then used to calculate improved values. During the corrector step, the nonlinear coefficients are evaluated using the most recently computed flow variables. Overall, second-order accurate solutions are obtained at the cost of two scalar bidiagonal and four scalar tridiagonal matrix inversions per streamwise station.

Near and in reversed-flow regions, the boundary-layer equations are solved in the inverse mode to avoid saddle-point behavior at the separation point. Here, the wall shear stress τ_w and the wake-centerline velocity u_{wc} are used as the inverse forcing functions because they can be simply and efficiently implemented. Also, flow-dependent difference operators are used in the reversed-flow regions to accommodate the required upstream influence.

If τ_w falls below a prescribed value the viscous algorithm converts from the direct to the inverse mode from that point on, including the entire wake. When operating in the inverse mode τ_w or u_{wc} must be updated so that the viscous and inviscid pressures converge. This is achieved with the interaction algorithms presented in Fig. 3. A transpiration velocity is used to introduce the influence of the viscous region upon the inviscid flow. After δ^* has been calculated, the transpiration

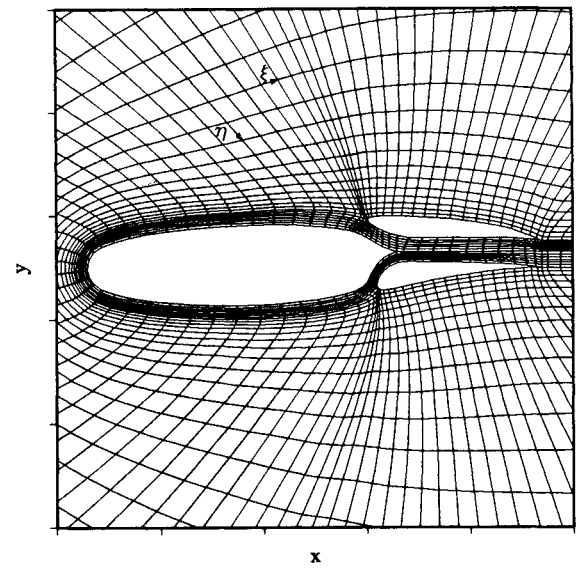

Fig. 1 Augmentor-wing finite-difference grid.

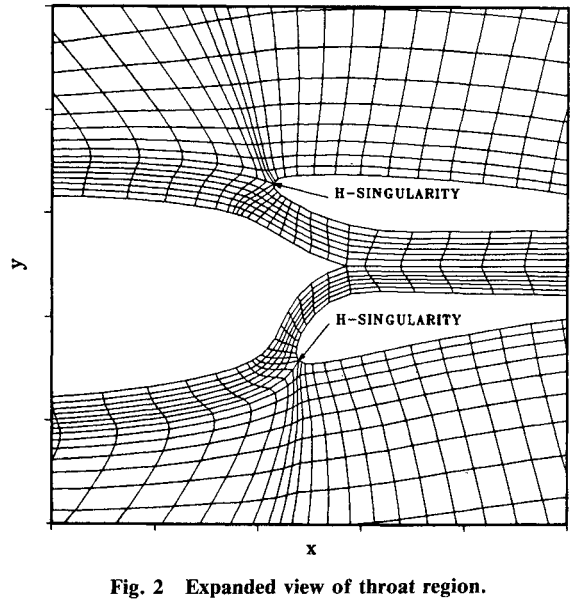

Fig. 2 Expanded view of throat region.

velocity is computed and then converted to the required perturbations of the inviscid contravariant velocities used in the inviscid algorithm. This approach allows the use of inviscid grids that are not orthogonal to a body surface or wake centerline in interaction codes. A viscous flow curvature correction is also included (using the procedure of Lock and Firmin[14]) in the six boundary layers and three wakes present in this geometry. The complete interaction scheme is summarized in Fig. 3 and further details of the viscous and viscous-inviscid interation algorithms can be found in Refs. 7-9.

Results

Initially, the cases presented here were run on a 106×35 inviscid grid. The cases were then rerun on a fine 226×60 inviscid grid. Small changes were observed in the pressure distributions due to the different inviscid grids. Furthermore, small separation regions not captured with the coarse grid (but observed in the Navier-Stokes results) were captured with the finer grid. However, overall the solution did not change greatly when the inviscid grid was refined by a factor of two, indicating grid independence. Only the 226×60 inviscid grid results are shown here.

The inviscid grid spacing along the bodies and wake centerline is also used in the viscous grids, which have 50 points in the direction normal to the body surfaces or wake centerlines. It should be pointed out that the number of points in the normal direction in the viscous grid is independent of the inviscid grid. Only the number of points along the body and wake centerline are changed to correspond one-to-one with the inviscid grid. In the viscous grid, the first point above the body is placed at approximately $y^+ = 2$. Viscous results are compared with the results of the inviscid computations[5] and experimental data[15] in Fig. 4 at cruise conditions (i.e., $M_\infty = 0.7$, $\alpha = 1.05$ deg, and $Re = 12.6 \times 10^6$). Upward- and downward-facing triangles denote experimental data for the upper and lower surfaces, respectively. The C_p distributions for the upper and lower shrouds have been displaced by $+1$ and -1, respectively. There is also a shift to the right in x/c for the data of the shrouds. The solid lines represent the viscous results and the dashed lines the inviscid. On the main airfoil, forward of the inlets, little change occurs in the C_p due to viscosity. This is expected, since in this region the effects of viscosity are negligible. The crossover of the C_p of the upper and lower surfaces is nicely captured for both inviscid and viscous flows. For inviscid flow, the trailing-edge C_p tends to the stagnation pressure, whereas the viscous result indicates a smaller pressure recovery. The viscous C_p exhibits a slight improvement over the inviscid solution near the aft portion of the main airfoil. There is a strong viscous/inviscid interaction in this region due to the thick, separated boundary layer on the main airfoil.

On the upper shroud, there is general improvement everywhere as compared to the inviscid solution. On the lower surface of the upper shroud, there is a significant improvement in C_p due to the accelerated flow in the channel region. This accelerated flow arises due to the thick, separated boundary layer/wake coming off the main airfoil. That is, the displacing effect of the boundary layers creates a smaller accelerated inviscid core in the channel region. In particular, there is a large improvement in accuracy in the upper inlet region (i.e., the region bounded by the lower surface of the upper shroud and the upper surface of the main airfoil). On the upper surface of the upper shroud, near the leading edge, there is a small improvement in C_p, as expected.

On the upper surface of the lower shroud, the effects of the accelerated flow in the channel region can be noticed. In particular, near the leading edge and in the throat region, the viscous C_p is higher than the inviscid C_p and compares favorably with the experimental data. On the lower surface, the viscous and inviscid C_p are almost identical, as expected. It appears that the major influence of viscosity is felt in those flow regions where there is a strong interaction between the various boundary layers. Other regions, such as the forward portion of the main airfoil, appear not to show any significant changes in C_p due to viscosity. Overall, the solution is in fair agreement with experimental data and the effects of viscosity are clearly illustrated for the cruise conditions.

Figure 5 compares the present viscous results to Navier-Stokes results.[6] The dashed lines are Navier-Stokes results and the solid lines the current ones. On the main airfoil, the pres-

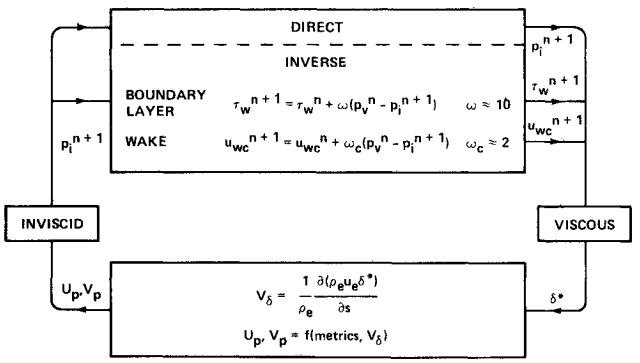

Fig. 3 Inviscid/viscous interaction flowchart.

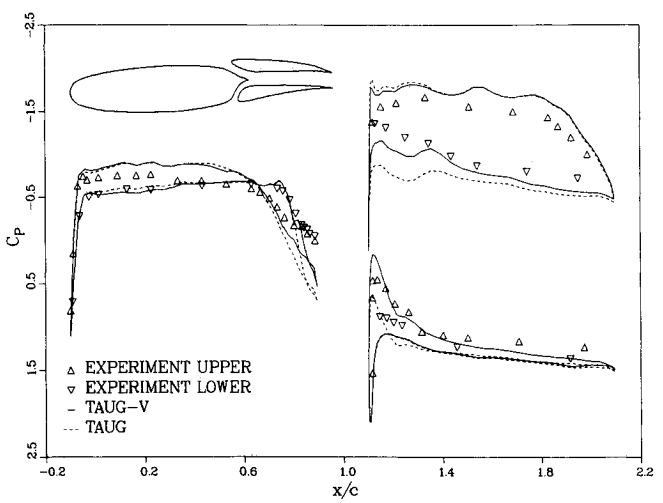

Fig. 4 Comparison of viscous/inviscid and inviscid C_p distributions: $M_\infty = 0.7$, $\alpha = 1.05$ deg, $Re = 12.6 \times 10^6$.

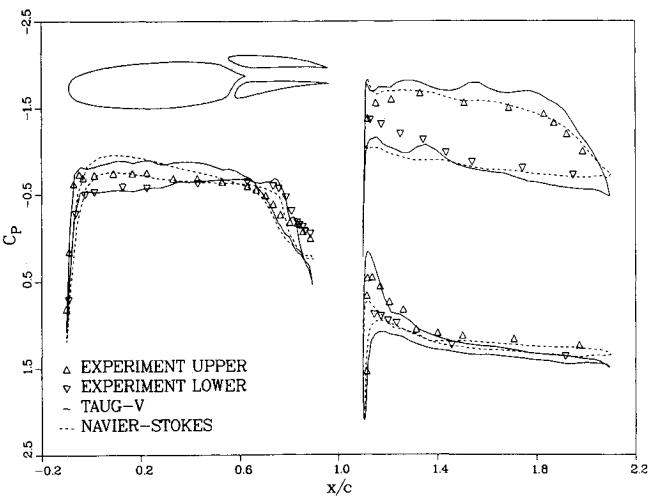

Fig. 5 Comparison of Navier-Stokes and viscous/inviscid C_p distributions: $M_\infty = 0.7$, $\alpha = 1.05$ deg, $Re = 12.6 \times 10^6$.

ent results compare much better with experimental data than the Navier-Stokes results. However, this is believed to be due to some shortcoming of the Navier-Stokes code, since the present code should not be expected to produce a better solution, just a less expensive one. The trailing-edge region C_p distributions are in fair agreement with each other, but slightly lower than experiment. The Navier-Stokes solution generally compares more favorably with experimental data than the present computations over most of the shrouds. However, in the upper inlet region on the lower surface of the upper shroud, the current results are in better agreement with the experimental data than the Navier-Stokes results. In the lower inlet region (defined similar to the upper inlet area), the present results are in better agreement with experimental data, because the Navier-Stokes computation failed to pick up the peak C_p at the leading edge. Both the present and Navier-Stokes results differ from the experimental data at the trailing edge of the main airfoil and on the lower surface of the upper shroud near the leading edge. This indicates that the boundary-layer assumptions are not responsible; however, it is possible that the influence of high curvature on the turbulence is not being properly modeled. (The Baldwin-Lomax turbulence model was used for the Navier-Stokes calculations, while the Cebeci-Smith turbulence model was used for the current results. Both models do not accuarately account for the influence of high curvature on the turbulence.) The present results are roughly equivalent to the Navier-Stokes results in terms of accuracy, but are obtained in roughly 1-2% of the CPU time required by the Navier-Stokes algorithm.

Additional insight into the nature of this flow is obtained from the boundary-layer velocity-vector plots of Fig. 6. The length and orientation of the arrows at each grid point (x,y) are proportional to the velocity vector. Figure 6a is a closeup view of the throat region. In the lower inlet, a thick, separated boundary layer exists on the lower surface of the main airfoil. This thick boundary layer (and to some extent the relatively thin separated boundary layer on the upper surface of the lower shroud) has accelerated the inviscid flow in this narrow channel and increases the leading-edge suction peak on the upper surface of the lower shroud. For purposes of illustrating the separation region, the velocity vectors at the trailing edge of the main airfoil are magnified by a factor of four, while the geometry is drawn to scale in Fig. 6b. Notice from Fig. 6b that the separation region on the lower surface extends to more surface grid points and is thicker relative to the upper surface. The separation at the trailing edges of the main airfoil was also observed by the Navier-Stokes computations. The development of the boundary layer on both surfaces of the upper shroud are clearly illustrated.

At the trailing edge of the main airfoil, the development of the asymmetric wake region is evident in Fig. 6a. Figure 6c shows the further development of the wake region of the main element and the boundary-layer development on the shrouds. The apparent "misalignment" of the shroud boundary layers and the wake of the main airfoil is due to the boundary-layer grids being adapted to each individual element (this is to be expected and is not an error). As the flow leaves the trailing edges of the shrouds, wakes are observed to develop and merge with the main airfoil wake. A small separation region occurs on the upper surface of the upper shroud near the trailing edge, which was also observed by the Navier-Stokes computations. In the preliminary results computed on the coarse grid, the separation on the upper surface of the main and upper shrouds was not captured. However, in refining the mesh, the separation regions did evolve and agree qualitatively with the Navier-Stokes results. Notice also, in contrast to many viscous/inviscid algorithms, that a symmetrical wake is not assumed.

To demonstrate the range of the present code, a strong shock case was computed. The flow conditions were $M_\infty = 0.649$, $\alpha = 4.7$ deg, $Re = 12.6 \times 10^6$ for both computations and experiment. Figure 7 compares the inviscid and viscous results

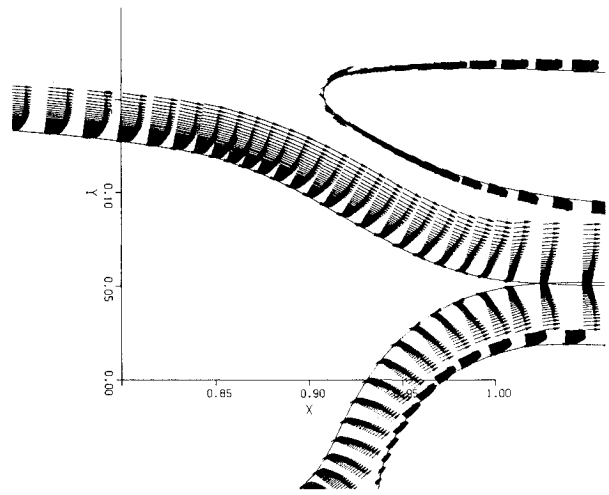

Fig. 6a Viscous velocity vectors in throat region: $M_\infty = 0.7$, $\alpha = 1.05$ deg, $Re = 12.6 \times 10^6$.

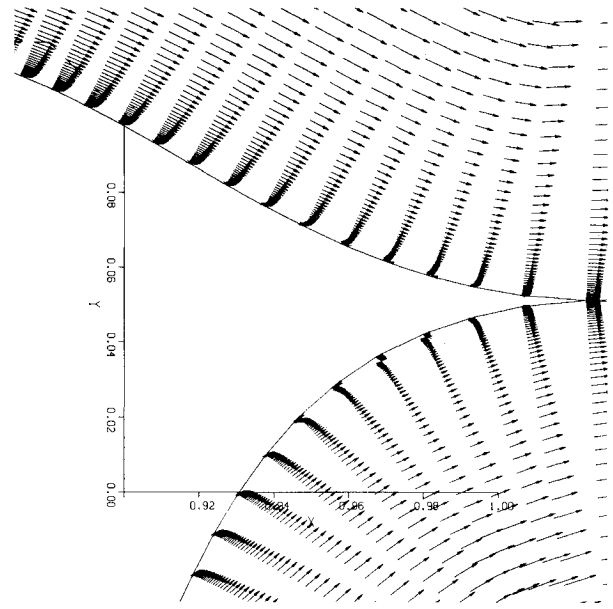

Fig. 6b Viscous velocity vectors magnified by four: $M_\infty = 0.7$, $\alpha = 1.05$ deg, $Re = 12.6 \times 10^6$.

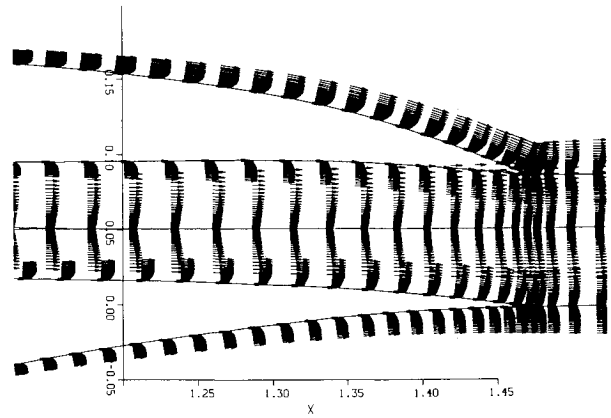

Fig. 6c Viscous velocity vectors near channel exit: $M_\infty = 0.7$, $\alpha = 1.05$ deg, $Re = 12.6 \times 10^6$.

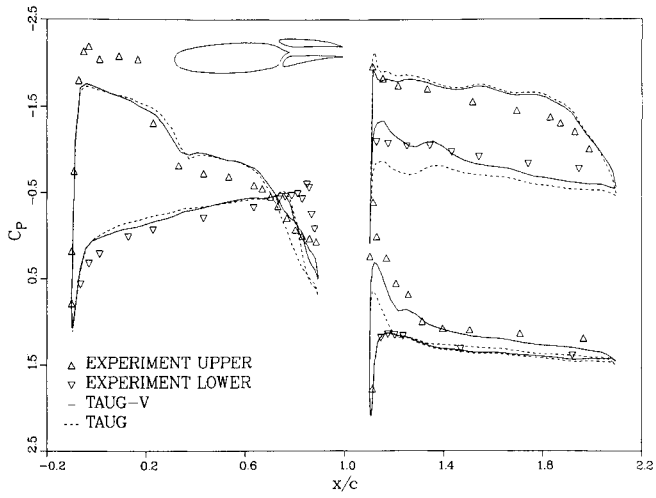

Fig. 7 Comparison of viscous/inviscid and inviscid C_p distributions: $M_\infty = 0.649$, $\alpha = 4.77$ deg, $Re = 12.6 \times 10^6$.

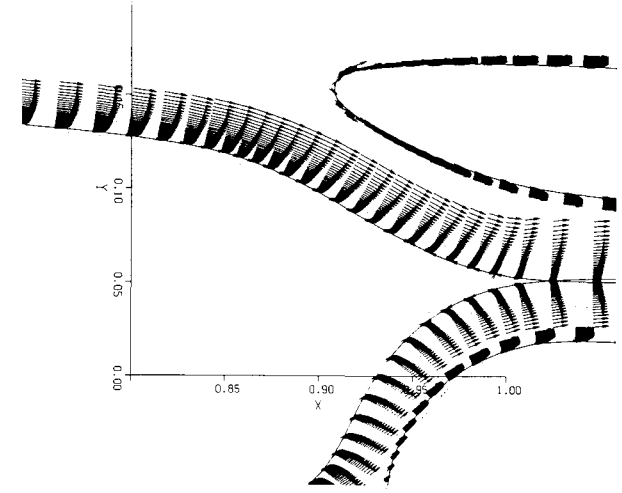

Fig. 8a Viscous velocity vectors in throat region: $M_\infty = 0.649$, $\alpha = 4.77$ deg, $Re = 12.6 \times 10^6$.

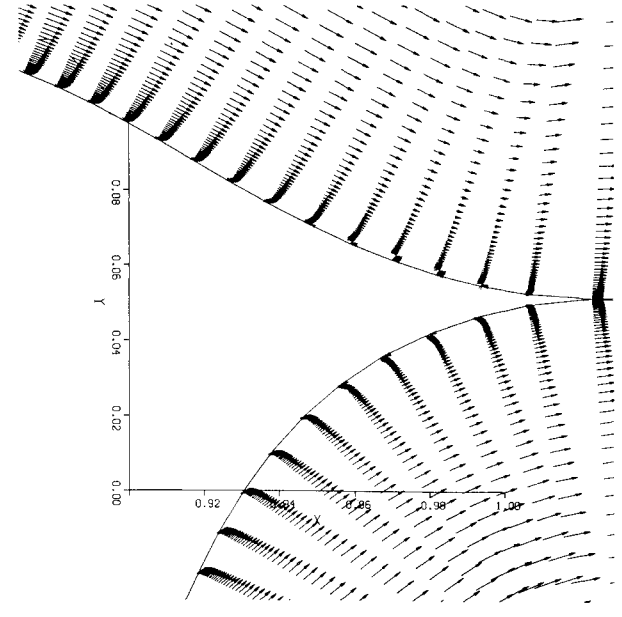

Fig. 8b Viscous velocity vectors magnified by four: $M_\infty = 0.649$, $\alpha = 4.77$ deg, $Re = 12.6 \times 10^6$.

with experiment. The solid lines represent the viscous results and the dashed lines the inviscid results. At this angle of attack, both the viscous and inviscid C_p underpredict the leading-edge pressure distribution. At the leading edge of the main airfoil, the effects of viscosity are small and the inviscid result should compare accurately with experiment. This underprediction of the leading-edge pressure by the inviscid result leads to the speculation that some error exists in the experiment due to wind tunnel/wall interference. Furthermore, only a small change occurred in the strength and location of the shock on the main airfoil due to viscosity effects. This same trend was also observed on coarse mesh calculations. The discrepancy with experiment for the coarse mesh results was thought to be partially attributed to the lack of grid resolution near the shock location. That is, better grid resolution would tend to sharpen the inviscid shock, which in turn would tend to feed a higher streamwise pressure gradient to the boundary layer. The subsequent stronger shock/boundary-layer interaction would move the viscous shock further upstream. However, there is real improvement in the portion of the main airfoil near the inlet regions. Significant improvements are also seen on the upper shroud, with good agreement between the viscous computations and experimental data in the inlet and leading-edge regions. On the lower shroud, there is a general overall improvement with very good agreement at the leading edge. In the channel region, due to the displacing effects of the boundary layers, the accelerated flow improves the accuracy of the results as compared to the inviscid solution. On all airfoils, the pressure recovery is lower as compared to the inviscid C_p.

It is interesting to note the qualitative difference in C_p around the leading edge on the upper shroud. For this case, on the upper surface, the leading edge C_p is greater compared to the cruise condition result, while on the lower surface the leading edge C_p relative to the result for the cruise condition is less. Recall that for the cruise conditions, the leading edge C_p matched for the upper shroud. These results indicate that, as we proceed around the leading edge onto the upper surface, there is an increased acceleration that produces a higher peak C_p (relative to the cruise conditions), whereas toward the lower surface from the leading edge, we see a deceleration which lowers the C_p. An explanation can be put forth by examining the viscous velocity vector plots of the surrounding inlet region shown in Fig. 8.

From Fig. 8a, we can see that a long separation region occurs on the upper surface of the main airfoil. (Contrast this with Fig. 6a for cruise conditions where a small separation region occured.) Intuitively from experience with single airfoils, it would be expected that the influence of the separation region in the upper inlet region would be to further accelerate the flow and increase the C_p on the lower surface of the upper shroud. However, this is in direct contrast to the experimental results of Fig. 7. Figure 8b is a magnification of the velocity vectors near the trailing edge of the main airfoil. The separation regions have an opposite trend as compared to Fig. 6b. Here, the larger separation region occurs on the upper surface, with a small separation occurring on the lower surface. Also, the length (i.e., number of surface grid points) of the separation region is greater on the upper surface than the lower surface. It is speculated that this large separation on the upper surface is what creates a thick boundary layer that diverts part of the flow in the upper inlet region to the upper surface. This explanation seems to be compatible with the observed increased acceleration on the upper surface of the upper shroud as indicated by Fig. 7.

These results are interesting since they lend insight into the complicated flow physics inherent in the augmentor wing. Generally, boundary-layer formation over a multielement configuration is highly influenced by the proximity of the various components. Also, when the spacing between the elements is small, the boundary layers may fill a large portion of the inner channels and have a magnified effect on the

aerodynamic characteristics as evidenced by this strong-shock case. However, with the present code, the effects of the boundary layers can be predicted as well as the answers to questions such as the effects of different spacings in the inlet and channel regions or flow separation on lift and drag coefficients.

Conclusions

The present code has demonstrated its ability to solve weak transonic and strong shock types of flow. It has been shown to handle both shock-induced and trailing-edge separation with relative ease. Besides being able to handle complex flows due to this unique geometry, the present code is practical. Roughly 1–4 min of Cray-XMP processor time is required to obtain a three-order magnitude drop in residuals. Little is known about interacting viscous/inviscid flow around multielement airfoils in the transonic regime or, in particular, with this type of configuration. For the design aerodynamacist who must consider many flow parameters as well as geometric configurations, the present code can play a major role in the preliminary design stages of the augmentor wing.

References

[1]"Analysis of Results from Test of an Asymmetric High Speed Augmentor-Wing Model (WTCB) in the NAE Two-Dimensional High Reynolds Number Blowdown Tunnel," The de Havilland Aircraft of Canada, Ltd., Rept. DHC-DIR 75-2, Aug. 1975.

[2]Whittley, D. C., "Augmentor-Wing Technology for STOL Transport Aircraft," Paper presented at High Lift Technology Course, University of Tennessee Space Institute, Tullahoma, Oct. 1975.

[3]Farbridge, J. E. and Smith, R. C., "The Transonic Multi Foil Augmentor-Wing," AIAA Paper 77-606, June 1977.

[4]Farbridge, J. E. and Whittley, D. C., "Some Aspects of Powerplant Airframe Integration Affecting Fuel Conservation," Paper presented at Canadian Symposium on Energy Conserving Transport Aircraft, Oct. 1977.

[5]Flores, J., Holst, T. L., and Sorenson, R. L., "Transonic Solutions for a Multielement Airfoil Using the Full-Potential Equations," *Journal of Aircraft*, Vol. 22, Jan. 1985, pp. 50–56.

[6]Lasinski, T. A., et al., "Computation of the Steady Viscous Flow over a Tri-Element 'Augmentor Wing' Airfoil," AIAA Paper 82-0021, Jan. 1982.

[7]Van Dalsem, W. R. and Steger, J. L., "Finite-Difference Simulation of Transonic Separated Flow Using a Full-Potential Boundary-Layer Interaction Approach," AIAA Paper 83-1689, July 1983.

[8]Van Dalsem, W. R., "Simulation of Separated Transonic Airfoil Flow by Finite-Difference Viscous-Inviscid Interaction," Ph.D. Thesis, Stanford University, Stanford, CA, June 1984.

[9]Van Dalsem, W. R. and Steger, J. L., "Simulation of Transonic Separated Airfoil Flow by Finite-Difference Viscous-Inviscid Interaction," presented at the Ninth International Conference on Numerical Methods in Fluid Dynamics, Saclay, France, June 25–29, 1984.

[10]Dougherty, F. C., Holst, T. L., Gundy, K. L., and Thomas, S. D., "TAIR—A Transonic Airfoil Analysis Computer Code," NASA TM-81296, 1981.

[11]Steger, J. L. and Sorenson, R. L., "Automatic Mesh-Point Clustering Near a Boundary in Grid Generation With Elliptic Partial Differential Equations," *Journal of Computational Physics*, Vol. 33, 1979, pp. 405–410.

[12]Sorenson, R. L., "A Computer Program to Generate Two-Dimensional Grids About Airfoils and Other Shapes by the Use of Poisson's Equation," NASA TM 81198, May 1980.

[13]Flores, J., Holst, T. L., Kwak, D., and Batiste, D. M., "A New Consistent Spatial Differencing Scheme for the Transonic Full Potential Equations," AIAA Paper 83-0373, Jan. 1983.

[14]Lock, R. C. and Firmin, M. C. P., "Survey of Techniques for Estimating Viscous Effects in External Aerodynamics," Royal Aeronautical Establishment, Tech. Rept. 1900, April 1981.

[15]Elfstrom, G. M., "Test on a 15 Chord Cruise Augmentor Model (WTCC) in the NAE 15″ × 60″ Test Facility," National Aeronautical Establishment (National Research Council Canada), Lab. Tech. Rept. LTR-HA-5X5/0100, March 1977.